Circuit quantum electrodynamics in the ultrastrong-coupling regime

T. Niemczyk[1]*, F. Deppe[1,2], H. Huebl[1], E. P. Menzel[1], F. Hocke[1], M. J. Schwarz[1], J. J. Garcia-Ripoll[3], D. Zueco[4], T. Hümmer[5], E. Solano[6,7], A. Marx[1] and R. Gross[1,2]

In circuit quantum electrodynamics[1-10] (QED), where superconducting artificial atoms are coupled to on-chip cavities, the exploration of fundamental quantum physics in the strong-coupling regime has greatly evolved. In this regime, an atom and a cavity can exchange a photon frequently before coherence is lost. Nevertheless, all experiments so far are well described by the renowned Jaynes–Cummings model[11]. Here, we report on the first experimental realization of a circuit QED system operating in the ultrastrong-coupling limit[12,13], where the atom–cavity coupling rate g reaches a considerable fraction of the cavity transition frequency ω_r. Furthermore, we present direct evidence for the breakdown of the Jaynes–Cummings model. We reach remarkable normalized coupling rates g/ω_r of up to 12% by enhancing the inductive coupling[14] of a flux qubit to a transmission line resonator. Our circuit extends the toolbox of quantum optics on a chip towards exciting explorations of ultrastrong light–matter interaction.

At microwave frequencies, strong coupling is feasible because of the enormous design flexibility of superconducting circuit QED systems[1,2]. Here, small cavity-mode volumes and large dipole moments of artificial atoms[15] enable coupling rates g of about[16,17] 1% of the cavity-mode frequency ω_r. Nevertheless, as in other systems[18-22], the quantum dynamics of these strongly coupled systems follows the Jaynes–Cummings model, which describes the coherent exchange of a single excitation between the atom and the cavity mode. Although the Hamiltonian of a realistic atom–cavity system contains so-called counter-rotating terms allowing the simultaneous creation or annihilation of an excitation in both, atom and cavity mode, these terms can be safely neglected for small normalized coupling rates g/ω_r. However, when g becomes a significant fraction of ω_r, the counter-rotating terms are expected to manifest, giving rise to exciting effects in QED. This ultrastrong-coupling regime is difficult to reach in quantum-optical cavity QED (refs 19,20), but was recently realized in a solid-state semiconductor system[23,24]. There, quantitative deviations from the Jaynes–Cummings model have been observed, but direct experimental proof of its breakdown by means of an unambiguous feature is still missing.

In this work, we exploit the potential of flux-based superconducting quantum circuits to reach the ultrastrong-coupling regime[13,14] and show direct evidence of physics beyond the Jaynes–Cummings model. To this end, we use the large nonlinear inductance of a Josephson junction shared between a flux qubit and a coplanar waveguide resonator. The transmission spectra of the combined system reveal qubit–mode couplings g/ω_r of up to 12% and anticrossings that cannot be explained by the Jaynes–Cummings model. Instead, they are caused by the simultaneous creation (annihilation) of two excitations, one in the qubit and one in a resonator mode, while annihilating (creating) only one excitation in a different resonator mode. The size of the anticrossings illustrates the importance of the counter-rotating terms for the qubit–cavity dynamics in the ultrastrong-coupling limit.

Images of our quantum circuit and a schematic of the measurement set-up are shown in Fig. 1. At a current antinode for the λ-mode of a niobium superconducting resonator (Fig. 1a–c), a part of the centre conductor is replaced with a narrow aluminium strip interrupted by a large-area Josephson junction (see the Methods section for fabrication details). This junction mediates most of the inductive coupling between a superconducting flux qubit[25] galvanically connected to the strip. The qubit consists of three nanometre-scaled Josephson junctions interrupting a superconducting loop, which is threaded by an external flux bias Φ_x. Scanning electron microscope (SEM) images of the qubit loop and the Josephson junctions are shown in Fig. 1d–f. For suitable junction sizes, the qubit potential landscape can be reduced to a double-well potential, where the two minima correspond to states with clockwise and anticlockwise persistent currents $\pm I_p$. At $\delta\Phi_x = \Phi_x - \Phi_0/2 = 0$, these two states are degenerate and separated by an energy gap Δ. In the qubit eigenbasis, the qubit Hamiltonian reads $\hat{H}_q = \hbar\omega_q\hat{\sigma}_z/2$. Here, $\omega_q = \sqrt{\Delta^2 + (2I_p \cdot \delta\Phi_x)^2}/\hbar$ is the qubit transition frequency, which can be adjusted by an external flux bias. We note, that for our flux qubit the two-level approximation is well justified because of its large anharmonicity. The resonator modes are described as harmonic oscillators, $\hat{H}_n = \hbar\omega_n(\hat{a}_n^\dagger\hat{a}_n + 1/2)$, where ω_n is the resonance frequency and n is the resonator-mode index. The operator $\hat{a}_n^\dagger$ ($\hat{a}_n$) creates (annihilates) a photon in the nth resonator mode. Owing to the inhomogeneous transmission line geometry[14] (see Fig. 1d), the higher mode frequencies of our resonator are not integer multiples of the fundamental resonance frequency ω_1. Throughout this work, we refer to the nth mode as the $n\lambda/2$-mode. Then, the Hamiltonian of our quantum circuit can be written as

$$\hat{H} = \hat{H}_q + \sum_n \left[\hat{H}_n + \hbar g_n \left(\hat{a}_n^\dagger + \hat{a}_n \right) (\cos\theta\,\hat{\sigma}_z - \sin\theta\,\hat{\sigma}_x) \right] \quad (1)$$

[1]Walther-Meißner-Institut, Bayerische Akademie der Wissenschaften, D-85748 Garching, Germany, [2]Physik-Department, Technische Universität München, D-85748 Garching, Germany, [3]Instituto de Física Fundamental, CSIC, Serrano 113-bis, 28006 Madrid, Spain, [4]Instituto de Ciencia de Materiales de Aragón and Departamento de Física de la Materia Condensada, CSIC-Universidad de Zaragoza, E-50009 Zaragoza, Spain, [5]Institut für Physik, Universität Augsburg, Universitätsstraße 1, D-86135 Augsburg, Germany, [6]Departamento de Química Física, Universidad del País Vasco - Euskal Herriko Unibertsitatea, Apdo. 644, 48080 Bilbao, Spain, [7]IKERBASQUE, Basque Foundation for Science, Alameda Urquijo 36, 48011 Bilbao, Spain.
*e-mail: thomas.niemczyk@wmi.badw.de.

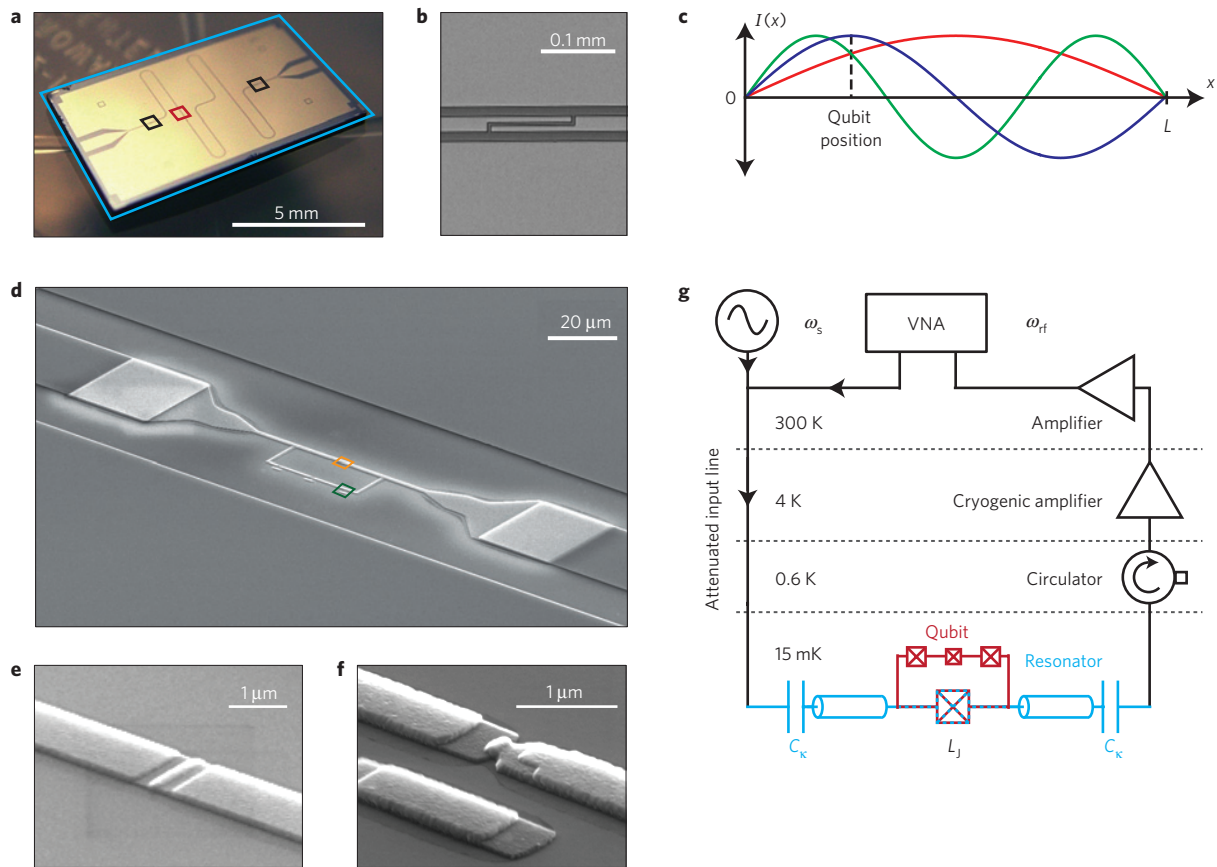**Figure 1 | Quantum circuit and experimental set-up. a**, Optical image of the superconducting $\lambda/2$ coplanar waveguide resonator (light blue rectangle). Black rectangles: area shown in **b**. Red rectangle: area shown in **d**. **b**, SEM image of one of the coupling capacitors. **c**, Sketch of the current distribution of the first three resonator modes. Their resonance frequencies are $\omega_1/2\pi = 2.782$ GHz ($\lambda/2$, red), $\omega_2/2\pi = 5.357$ GHz (λ, blue) and $\omega_3/2\pi = 7.777$ GHz ($3\lambda/2$, green). The cavity modes ω_n are measured at maximum qubit–cavity detuning ($\Phi_x = 0$). In general, the flux dependence of ω_n is very weak, except for the regions close to $\Phi_x = \pm\Phi_0/2$. **d**, SEM image of the galvanically coupled flux qubit (see the Methods section for fabrication details). The width in the overlap regions with the centre conductor is 20 μm, and that of the constriction is 1 μm. Orange rectangle: area shown in **e**. Green rectangle: area shown in **f**. **e**, SEM image of the large Josephson junction. Its Josephson inductance L_J is responsible for approximately 85% of the qubit–resonator coupling. **f**, One Josephson junction of the qubit loop. The area of this junction is 14% of the one shown in **e**. **g**, Schematic of the measurement set-up. The transmission through the cavity at ω_{rf} is measured using a vector network analyser (VNA). A second microwave signal at ω_s is used for two-tone qubit spectroscopy. The input signal is attenuated at various temperature stages and coupled into the resonator (light blue) through the capacitors C_K. The crossed squares represent Josephson junctions. A circulator isolates the sample from the amplifier noise.

Here, $\hat{\sigma}_{x,z}$ denote Pauli operators, g_n is the coupling rate of the qubit to the nth cavity mode and the flux dependence is encoded in $\sin\theta = \Delta/\hbar\omega_q$ and $\cos\theta$. The operator $\hat{\sigma}_x$ is conveniently expressed as the sum of the qubit raising ($\hat{\sigma}_+$) and lowering ($\hat{\sigma}_-$) operator. Thus, in contrast to the Jaynes–Cummings model, the Hamiltonian in equation (1) explicitly contains counter-rotating terms of the form $\hat{a}_n^\dagger\hat{\sigma}_+$ and $\hat{a}_n\hat{\sigma}_-$. Figure 1g shows a schematic of our measurement set-up. The quantum circuit is located at the base temperature of 15 mK in a dilution refrigerator. We measure the amplified resonator transmission using a vector network analyser. For qubit spectroscopy measurements, the system is excited with a second microwave tone ω_s with power P_s, while using the $3\lambda/2$-mode at $\omega_3/2\pi = 7.777$ GHz for dispersive readout[9,26].

We first present measurements allowing the extraction of the coupling constants of the qubit to the first three resonator modes. The spectroscopy data in Fig. 2a show the dressed qubit transition frequency[1,26] with the expected hyperbolic flux dependence and a minimum at $\delta\Phi_x = 0$. Furthermore, the two lowest resonator modes (ω_1 and ω_2) are visible. In principle, a fit to the Hamiltonian in equation (1) would yield all system parameters. However, our measurement resolution does not allow us to reliably determine the system parameters, in particular the undressed qubit energy

gap Δ and the coupling constants g_n in this situation. Instead, we extract them from a cavity transmission spectrum with negligible photon population. For that purpose, we first measure the power-dependent a.c.-Zeeman shift of the qubit transition frequency at $\delta\Phi_x = 0$. The data are shown in the inset of Fig. 2a. The average photon number $\bar{n}_3$ can be estimated using the relation $P_{rf} = \bar{n}_3\hbar\omega_3\kappa_3$ (refs 6,8), where $\kappa_3/2\pi \approx 3.7$ MHz is the full-width at half-maximum of the cavity resonance and P_{rf} is the probe power referred to the input of the resonator. Figure 2b shows a colour-coded transmission spectrum for the $3\lambda/2$-mode as a function of $\delta\Phi_x$. The data are recorded at an input power $P_{rf} \approx -140$ dBm (green data point in Fig. 2a, inset) corresponding to $\bar{n}_3 = 0.18$.

We observe a spectrum with a large number of anticrossings resulting from the multimode structure of our cavity system. To extract the individual coupling constants g_n, we compute the lowest nine transition frequencies of the Hamiltonian given in equation (1) incorporating the first three resonator modes. Fitting the results to the spectrum of the $3\lambda/2$-mode shows excellent agreement with the measured data as shown in Fig. 2c. We note that the spectrum for the λ-mode shown in Fig. 2d can be well described without additional fitting using the parameters extracted from the $3\lambda/2$-mode. For the qubit, we obtain $2I_p = 630$ nA
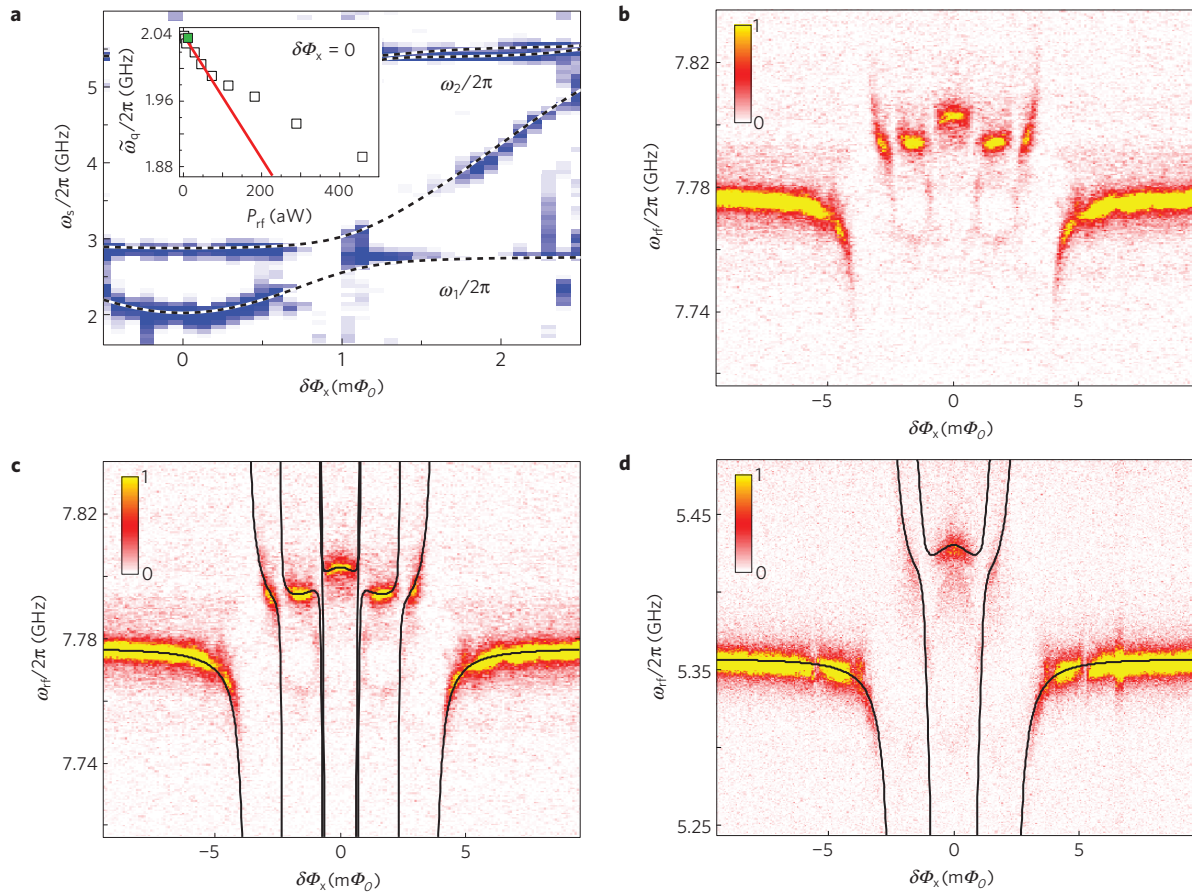
Figure 2 | Qubit microwave spectroscopy and low-power transmission spectra. a, Microwave spectroscopy of the coupled qubit–cavity system. The measured transmission magnitude (colour coded, blue: low; white: high) is plotted as a function of the relative flux bias $\delta\Phi_x$ and the spectroscopy frequency $\omega_s/2\pi$. The black dashed lines indicate the dressed[9,26] energy-level spectrum of Hamiltonian (1) obtained with the fit parameters from the cavity transmission data in Fig. 2c. Owing to the long acquisition time, we need to account for a small flux drift using a slightly smaller value for I_p. The spectrum is recorded at P_{rf} corresponding to $\bar{n}_3 \approx 0.5$. Near the anticrossing regions with the two lowest cavity modes, the transmitted signal through the readout mode ω_3 disappears in the noise floor. Inset: Centre frequency of the qubit spectroscopy signal at $\delta\Phi_x = 0$ as a function of the probe power P_{rf}. The full-width at half-maximum of the qubit signal is approximately 80 MHz in the low-power limit $P_{rf}, P_s \to 0$. Red line: fit to the linear region[30]. The green dot indicates the power level at which the spectra in **b,c** and Fig. 3 are recorded. **b**, Cavity transmission ($3\lambda/2$-mode, linear scale, arbitrary units) as a function of $\delta\Phi_x$ and probe frequency $\omega_{rf}/2\pi$. **c**, The same spectrum as in **b**. Black lines: numerical fit of the spectrum of the Hamiltonian (1) to the data. **d**, Cavity transmission (λ-mode, linear scale, arbitrary units) as a function of $\delta\Phi_x$ and probe frequency $\omega_{rf}/2\pi$. The spectrum is recorded at P_{rf} corresponding to $\bar{n}_2 \approx 0.9$ because of a higher insertion loss of this cavity mode. Black lines: numerically evaluated energy-level spectrum with parameters from **c**.

and $\Delta/h = 2.25$ GHz. The latter deviates significantly from the dressed qubit transition frequency $\tilde{\omega}_q$ at $\delta\Phi_x = 0$ (see Fig. 2a, inset) because of the strong qubit–cavity interaction. Most importantly, we find coupling rates of $g_1/2\pi = 314$ MHz, $g_2/2\pi = 636$ MHz and $g_3/2\pi = 568$ MHz. The values for g_n correspond to normalized coupling rates g_n/ω_n of remarkable 11.2%, 11.8% and 7.3%, respectively. These large coupling rates allow us to enter the ultrastrong-coupling regime and, as we will show below, lead to significant deviations from the Jaynes–Cummings physics.

In the following, we analyse the features in our data that constitute unambiguous evidence for the breakdown of the rotating-wave approximation inherent to the Jaynes–Cummings model. In Fig. 3, we compare the energy-level spectrum of the Hamiltonian in equation (1) with that of a three-mode Jaynes–Cummings model. We note that, depending on $\delta\Phi_x$, there are regions where our data can be well described by the Jaynes–Cummings model, and regions where there are significant deviations (see Fig. 3a). For our analysis we use the notation $|q, N_1, N_2, N_3\rangle = |q\rangle \otimes |N_1\rangle \otimes |N_2\rangle \otimes |N_3\rangle$, where $q = \{g, e\}$ denote the qubit ground or excited state, respectively, and $|N_n\rangle = \{|0\rangle, |1\rangle, |2\rangle, \ldots\}$ represents the Fock state with photon

occupation N in the nth resonator mode. At the outermost anticrossings (Fig. 3b), where $\omega_3 \approx \omega_q$, the eigenstates $|\psi_\pm\rangle$ of the coupled system are in good approximation symmetric and antisymmetric superpositions of $|e, 0, 0, 0\rangle$ and $|g, 0, 0, 1\rangle$. This exchange of a single excitation between the qubit and the resonator is a characteristic of the Jaynes–Cummings model. On the contrary, the origin of the anticrossing shown in Fig. 3c is of a different nature: the dominant contributions to the eigenstates $|\psi_\pm\rangle$ are approximate symmetric and antisymmetric superpositions of the degenerate states $\varphi_1 = |e, 1, 0, 0\rangle$ and $\varphi_2 = |g, 0, 0, 1\rangle$. The transition from φ_1 to φ_2 can be understood as the annihilation of two excitations, one in the $\lambda/2$-mode and one in the qubit, while, simultaneously, creating only one excitation in the $3\lambda/2$-mode. Such a process can result only from counter-rotating terms as they are present in the Hamiltonian (1), but not within the Jaynes–Cummings approximation. Here, only eigenstates with an equal number of excitations can be coupled. Although counter-rotating terms in principle exist in any real circuit QED system, their effects become prominent only in the ultrastrong-coupling limit with large normalized couplings g_n/ω_n as realized in our system. Hence, the observed anticrossing shown in Fig. 3c

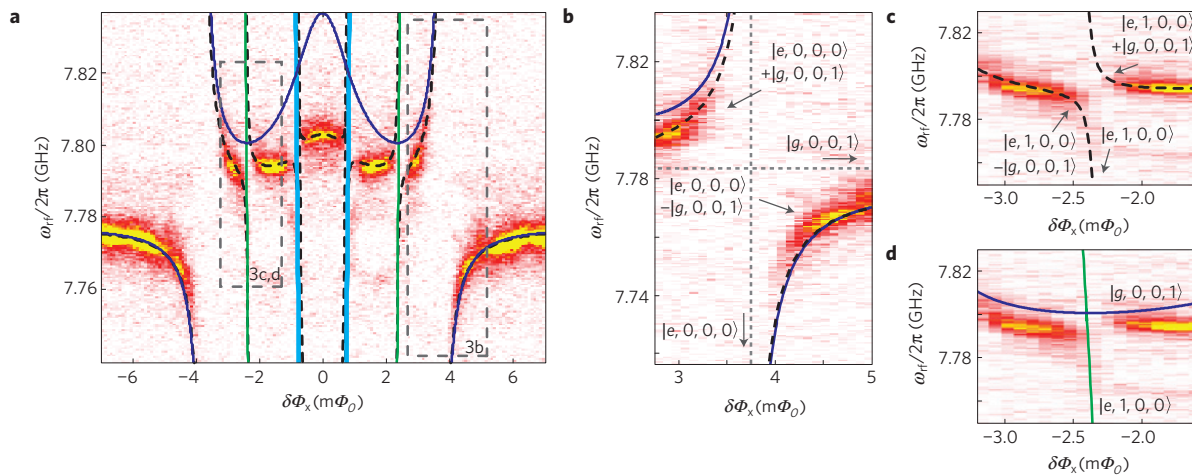**Figure 3 | Breakdown of the Jaynes–Cummings model. a**, Cavity transmission ($3\lambda/2$-mode, linear scale, arbitrary units) as a function of $\delta\Phi_x$ and probe frequency $\omega_{rf}/2\pi$. Black dashed lines in all plots: energy-level spectrum obtained from the Hamiltonian (1). Coloured lines in all plots: energy-level spectrum obtained from the Jaynes–Cummings model (dark blue: $|g, 0, 0, 1\rangle$, except for anticrossing region shown in **b**; green: $|e, 1, 0, 0\rangle$; light blue: $|e, 0, 1, 0\rangle$ and $|e, 2, 0, 0\rangle$, which are indistinguishable within the resolution of this plot. Grey dashed rectangle: areas magnified in **b–d**. **b**, Single excitation anticrossing. The quantitative deviations of the Jaynes–Cummings model from equation (1) are attributed to a small admixture of the state $|g, 1, 1, 0\rangle$. The uncoupled states are indicated by grey dashed lines. **c**, Avoided crossing resulting from a coupling between the degenerate states $|g, 0, 0, 1\rangle$ and $|e, 1, 0, 0\rangle$. This is caused by counter-rotating terms in the Hamiltonian (1). A detailed analysis yields a minor admixture of $|g, 1, 1, 0\rangle$ (superposition states: $\approx |g, 0, 0, 1\rangle/\sqrt{2} \pm (|e, 1, 0, 0\rangle/\sqrt{3} + |g, 1, 1, 0\rangle/\sqrt{6})$). This admixture has no effect on the reasoning presented in the main text. The energy-level spectrum obtained from the Jaynes–Cummings model is omitted for clarity. The dominant contributions to the superposition states of the innermost anticrossings in Fig. 2d are $|g, 0, 1, 0\rangle$, $|g, 2, 0, 0\rangle$ and $|e, 1, 0, 0\rangle$. **d**, The same as in **c**, but for the Jaynes–Cummings model. Within numerical accuracy, no anticrossing is predicted, clearly contradicting the data.

is a direct experimental manifestation of physics beyond the rotating-wave approximation in the Jaynes–Cummings model. As shown in Fig. 3d, the latter would imply a crossing of the involved energy levels, which is not observed. A similar argument applies to the innermost anticrossings of the $3\lambda/2$-mode (see Fig. 3a), although the involved eigenstates have a more complicated character, and to the innermost anticrossings of the λ-mode shown in Fig. 2d.

We have presented measurements on a superconducting circuit QED system in the ultrastrong-coupling regime. Our transmission spectra are in excellent agreement with theoretical predictions and show clear evidence for physics beyond the Jaynes–Cummings model. This system can act as an on-chip prototype for unveiling the physics of ultrastrong light–matter interaction. Future explorations may include squeezing, causality effects in quantum field theory[27], the generation of bound states of qubits and photons[28], *in situ* switching of distinct physical regimes[29] and ultrafast quantum operations in circuit QED for quantum information protocols.

Methods

Fabrication details. The coplanar waveguide resonator is fabricated using optical lithography and reactive ion etching. We use a thermally oxidized (50 nm) silicon substrate with a 100-nm-thick niobium film, deposited by d.c.-magnetron sputtering before patterning. The coplanar waveguide centre conductor is $20\,\mu m$ wide and separated from the lateral ground planes by a gap of $12\,\mu m$, resulting in a characteristic impedance of approximately $50\,\Omega$. The resonator with a length of 23 mm is defined by two interdigital coupling capacitors (see Fig. 1b) with a numerically calculated capacitance of about 10 fF. The centre conductor is interrupted by a gap of $80\,\mu m$ at a maximum of the current distribution for the λ-mode (see Fig. 1c). At this point, the amplitude of the standing current wave for the $\lambda/2$- and $3\lambda/2$-mode is smaller by a factor of $1/\sqrt{2}$. The aluminium strip connected to the flux qubit and the large Josephson junction is fabricated by electron-beam lithography and Al/AlO$_x$/Al shadow evaporation techniques. For the bottom and top aluminium layer, we use a thickness of 50 and 80 nm, respectively. For the *in situ* oxidation of the bottom layer, pure oxygen ($p_{O_2} = 2 \times 10^{-4}$ mbar; 22 min) is used. Two of the qubit Josephson junctions have an area $A \approx 250 \times 140\,nm^2$ whereas the other junction is smaller by a factor of $\alpha \approx 0.7$. The critical current density of the Josephson junctions is $j_c \approx 1.3$ kA cm^{-2}, leading to a Josephson energy of $E_J \approx 224$ GHz for a junction with area A. The area

of the qubit loop is roughly $20 \times 9\,\mu m^2$ and the large Josephson junction mediating the ultrastrong qubit–cavity coupling has an area of about $7A$.

Theoretical description of the coupling. The qubit–cavity coupling is determined by the local inductance $M = L_J + L$. Here, L_J is the Josephson inductance of the coupling junction and L is the inductance of the shared edge between the centre conductor and the qubit. Although $L_J > L$ dominates M, it has negligible influence on the vacuum current $I_n \approx \sqrt{\hbar\omega_n/L_r}$ in the resonator because the total resonator inductance $L_r \gg L_J, L$. Consequently, the coupling strengths can be written as $\hbar g_n = MI_nI_p$. This result can also be obtained analytically from a more thorough theoretical treatment[14]. From the experimental values of g_n, we obtain $L_J \approx 60$ pH in agreement with our junction parameters.

References

1. Blais, A., Huang, R-S., Wallraff, A., Girvin, S. M. & Schoelkopf, R. J. Cavity quantum electrodynamics for superconducting electrical circuits: An architecture for quantum computation. *Phys. Rev. A* **69**, 062320 (2004).
2. Wallraff, A. *et al.* Strong coupling of a single photon to a superconducting qubit using circuit quantum electrodynamics. *Nature* **431**, 162–167 (2004).
3. Chiorescu, I. *et al.* Coherent dynamics of a flux qubit coupled to a harmonic oscillator. *Nature* **431**, 159–162 (2004).
4. Johansson, J. *et al.* Vacuum Rabi oscillations in a macroscopic superconducting qubit LC oscillator system. *Phys. Rev. Lett.* **96**, 127006 (2006).
5. Schuster, D. I. *et al.* Resolving photon number states in a superconducting circuit. *Nature* **445**, 515–518 (2007).
6. Astafiev, O. *et al.* Single artificial-atom lasing. *Nature* **449**, 588–590 (2007).
7. Deppe, F. *et al.* Two-photon probe of the Jaynes–Cummings model and controlled symmetry breaking in circuit QED. *Nature Phys.* **4**, 686–691 (2008).
8. Fink, J. *et al.* Climbing the Jaynes–Cummings ladder and observing its $\sqrt{n}$ nonlinearity in a cavity QED system. *Nature* **454**, 315–318 (2008).
9. Abdumalikov, A., Astafiev, O., Nakamura, Y., Pashkin, Y. & Tsai, J. Vacuum Rabi splitting due to strong coupling of a flux qubit and a coplanar-waveguide resonator. *Phys. Rev. B* **78**, 180502 (2008).
10. Hofheinz, M. *et al.* Synthesizing arbitrary quantum states in a superconducting resonator. *Nature* **459**, 546–549 (2009).
11. Jaynes, E. T. & Cummings, F. W. Comparison of quantum and semiclassical radiation theories with application to the beam maser. *Proc. IEEE* **51**, 89–109 (1963).

12. Ciuti, C. & Carusotto, I. Input–output theory of cavities in the ultrastrong coupling regime: The case of time-independent cavity parameters. *Phys. Rev. A* **74,** 033811 (2006).
13. Devoret, M., Girvin, S. & Schoelkopf, R. Circuit-QED: How strong can the coupling between a Josephson junction atom and a transmission line resonator be? *Ann. Phys.* **16,** 767–779 (2007).
14. Bourassa, J. *et al*. Ultrastrong coupling regime of cavity QED with phase-biased flux qubits. *Phys. Rev. A* **80,** 032109 (2009).
15. Niemczyk, T. *et al*. Fabrication technology of and symmetry breaking in superconducting quantum circuits. *Supercond. Sci. Technol.* **22,** 034009 (2009).
16. Schoelkopf, R. J. & Girvin, S. M. Wiring up quantum systems. *Nature* **451,** 664–669 (2008).
17. Bishop, L. *et al*. Nonlinear response of the vacuum Rabi resonance. *Nature Phys.* **5,** 105–109 (2008).
18. Thompson, R. J., Rempe, G. & Kimble, H. J. Observation of normal-mode splitting for an atom in an optical cavity. *Phys. Rev. Lett.* **68,** 1132–1135 (1992).
19. Walther, H., Varcoe, B. T. H., Englert, B-G. & Becker, T. Cavity quantum electrodynamics. *Rep. Prog. Phys.* **69,** 1325–1382 (2006).
20. Haroche, S. & Raimond, J-M. *Exploring the Quantum* (Oxford Univ. Press, 2006).
21. Reithmaier, J. P. *et al*. Strong coupling in a single quantum dot semiconductor microcavity system. *Nature* **432,** 197–200 (2004).
22. Gröblacher, S., Hammerer, K., Vanner, M. R. & Aspelmeyer, M. Observation of strong coupling between a micromechanical resonator and an optical cavity field. *Nature* **460,** 724–727 (2009).
23. Günter, G. *et al*. Sub-cycle switch-on of ultrastrong light–matter interaction. *Nature* **458,** 178–181 (2009).
24. Anappara, A. *et al*. Signatures of the ultrastrong light–matter coupling regime. *Phys. Rev. B* **79,** 201303 (2009).
25. Mooij, J. E. *et al*. Josephson persistent-current qubit. *Science* **285,** 1036–1039 (1999).
26. Schuster, D. I. *et al*. Ac stark shift and dephasing of a superconducting qubit strongly coupled to a cavity field. *Phys. Rev. Lett.* **94,** 123602 (2005).
27. Sabin, C., Garcia-Ripoll, J. J., Solano, E. & Leon, J. Dynamics of entanglement via propagating microwave photons. *Phys. Rev. B* **81,** 184501 (2010).
28. Hines, A. P., Dawson, C. M., McKenzie, R. H. & Milburn, G. J. Entanglement and bifurcations in Jahn-Teller models. *Phys. Rev. A* **70,** 022303 (2004).
29. Peropadre, B., Forn-Diaz, P., Solano, E. & Garcia-Ripoll, J. J. Switchable ultrastrong coupling in circuit QED. *Phys. Rev. Lett.* **105,** 023601 (2010).
30. Zueco, D., Reuther, G. M., Kohler, S. & Hanggi, P. Qubit-oscillator dynamics in the dispersive regime: Analytical theory beyond the rotating-wave approximation. *Phys. Rev. A* **80,** 033846 (2009).

Author contributions

T.N. fabricated the sample, conducted the experiment and analysed the data presented in this work. F.D. provided important contributions regarding the interpretation of the results. T.N. and F.D. co-wrote the manuscript. J.J.G-R. provided the basic idea and the techniques for the numerical analysis of the data. E.S. and J.J.G-R. supervised the interpretation of the data. D.Z. and T.H. contributed to the understanding of the results and developed an analytical model of our system. H.H. contributed to the numerical analysis and helped with the experiment. E.P.M. contributed strongly to the experimental set-up. M.J.S. and F.H. contributed to discussions and helped edit the manuscript. A.M. and R.G. supervised the experimental part of the work.